

Chapter Three

Growth of b-axis-oriented Rare Earths

3.1 Overview

This Chapter describes the growth of b-axis-oriented rare earths. The procedure is complicated and its development required two years of experimental effort. In contrast to the MBE growth of c-axis-oriented rare earths, which happen to be straightforward and forgiving of non-optimal growth parameters, the successful growth of b-axis-oriented rare earths requires precise growth parameters and careful control of growth conditions. This is the case because the basal plane is generally the low energy habit plane for hcp metals, and is therefore preferred over alternative surface planes. The procedure requires the growth and refinement of six distinct buffer layers and interfaces, and as such is certainly the most complicated sequence used to date for the preparation of oriented metal multilayers.

The growth conditions are reported here in some detail because these are complicated structures and the ultimate refinement of the growth parameters required detailed knowledge of each layer. The optimal growth conditions turn out to be quite different from those employed for c-axis-oriented rare earth samples and hold intrinsic interest insofar as they reveal some of materials physics involved in these systems. Also, the expected magnetic properties of b-axis-oriented rare earths are coupled directly to their structural properties. A detailed knowledge of film growth and microstructure could therefore be useful for an interpretation of the magnetic properties.

The Chapter is organized as follows. Following a brief overview of the growth

procedure, background material about epitaxial growth modes and techniques for overcoming lattice mismatch are given. These place subsequent experimental observations and procedures into perspective. Subsequent Sections provide full details about the growth and characterization of the substrate and buffer layers used for b-axis-oriented rare earths.

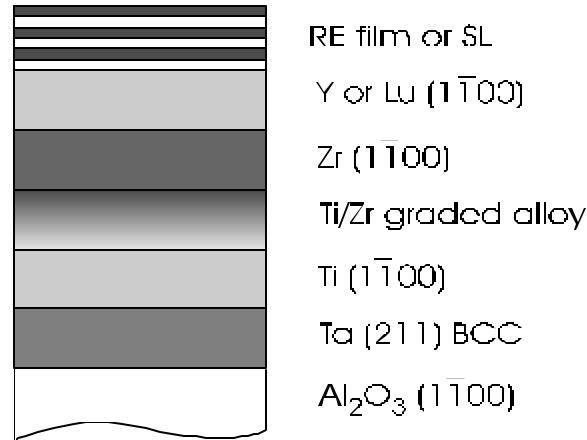


Figure 3.1: Schematic cross-section of a b-axis-oriented rare earth thin film, showing the Ti layer which selects the desired orientation, and the compositionally-graded Zr/Ti layer which achieves better lattice misfit with the rare earths.

Overview

The procedure developed to produce b-axis-oriented rare earth thin films stems directly from the discovery by Huang and Flynn that single-crystal hcp Ti can be grown in six chosen crystallographic orientations [1], including the $(1\bar{1}00)$ surface of interest here. The growth procedure involves three steps: First, the desired symmetry and crystallographic direction is selected by the growth of hcp Ti($1\bar{1}00$) on a buffer layer of bcc Ta(211) grown on M-plane sapphire [2]. Second, the 20% lattice misfit between the rare earths and Ti is partially relieved by means of an intermediate Zr buffer layer. Since Ti and Zr are mutually miscible but have 10% lattice misfit, Zr is slowly graded into Ti, forming a variable composition alloy, until a thick layer of pure single-crystal Zr($1\bar{1}00$) is obtained. This is then followed by heteroepitaxial deposition of Lu under conditions which

overcome the remaining 10% lattice misfit.

Tunably-strained Dy is achieved by growth on alloys of Y and Lu. These materials are important buffer layer materials for the growth of the magnetic rare earths [3]. They are structurally and chemically similar and provide ideal templates for the synthesis of high-quality magnetic thin films. Moreover, their mutual solubility and their convenient location on opposite sides of the lanthanide series enables these materials, via the lanthanide contraction, to be alloyed and used to synthesize magnetic layers with tuned strain. A schematic cross section of a sample appears in Figure 3.1.

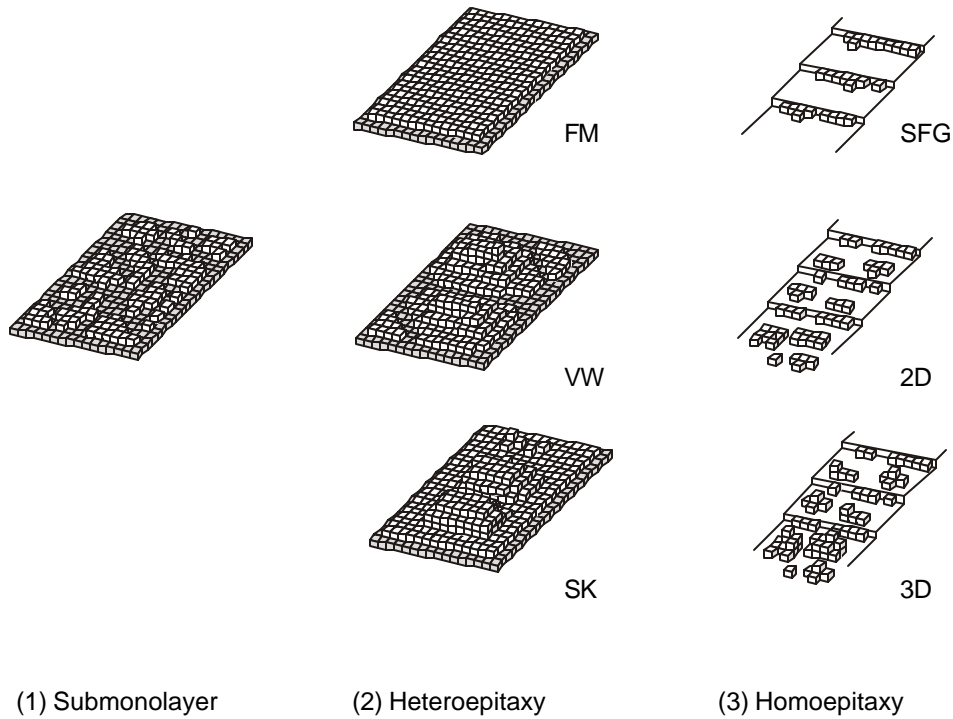


Figure 3.2: Schematic representation of the regimes of heteroepitaxial growth, showing the various growth modes associated with each. The abbreviations are defined in the text.

Growth Mode Considerations

The heteroepitaxial growth of an epilayer on a substrate is naturally partitioned into the following three regimes: submonolayer coverage during initial deposition, heteroepitaxial nucleation and growth, and finally homoepitaxial growth [4]. The initial submonolayer range of heteroepitaxial growth remains complicated and there is no unified model to

describe observed behavior. The process is essentially chemisorption, and it therefore depends strongly on the specific chemical interaction between the substrate and adatoms [5]. In practice, dedicated experimental techniques are required to study this regime, and a detailed understanding of this regime is not necessary to grow b-axis-oriented rare earths.

The next stage is heteroepitaxial growth of an epilayer on a substrate and this usually occurs in one of three distinct growth modes, the proclivity for which can often be predicted by thermodynamic considerations [6]. The important thermodynamic variable which selects between these modes is the difference in film (f), substrate (s), and interfacial (i) surface free energy, $\Delta = \gamma_f + \gamma_i - \gamma_s$. The somewhat-idealized **Frank-van der Merwe (FM)** mode requires the wetting condition $\Delta \leq 0$ to be fulfilled for each successive monolayer [7],[8]. Characterized by smooth, layer-by-layer epitaxy, FM is scarcely realized in practice; in the presence of any lattice misfit, the growth becomes metastable against roughening and clustering [9],[10].

The **Volmer-Weber (VW)** mode, requiring $\Delta > 0$, involves the nucleation of three-dimensional atomic clusters on the substrate. Growth by this mode takes place when the epilayer-epilayer interaction is stronger than the epilayer-substrate interaction [11]. Finally, in the the **Stranski-Krastanov (SK)** mode, islands grow on a thin wetting layer with $\Delta \leq 0$ [12]. These are broad categories and, since the growth process is inherently a nonequilibrium one, there is often considerable overlap and additional complexity [5].

In the present research the Stranski-Krastanov growth mode occurs in the growth of Ti on Ta and Lu on Zr. For small thicknesses, the strained, wetting epilayer can reduce the free energy by completely covering the substrate. Strain energy increases with thickness, however, and beyond some critical thickness this energy can be reduced by the spontaneous formation of misfit dislocations.

Finally, when the epilayer growing on the substrate becomes sufficiently thick, and as the effects of the substrate diminish, the growth process becomes homoepitaxial. The two common modes of homoepitaxial growth are the layer-by-layer growth mode (encompassing both 2D and 3D regimes) and the step-flow growth (Burton-Cabrera-Frank)

mode [13],[14]. In the former, adatoms with limited mobility nucleate at terraces away from step edges. In the latter, adatoms diffuse freely to step edges where they nucleate, and the film grows by a continuous flow of steps [15]. An illustration of these categories of growth behavior appears in Figure 3.2. The layer-by-layer growth model is frequently accompanied by characteristic oscillations of RHEED specular intensity. These oscillations derive from the variation of surface roughness as each developing layer is progressively covered with atoms until completed. RHEED oscillations occur for the growth of Ti on Ta [16].

Overcoming Lattice Mismatch

Epitaxial growth of one material directly on another is generally only possible when the lattice parameters and symmetries of the materials are compatible. Otherwise, the lattice misfit destroys coherency and the resulting epilayer becomes polycrystalline or highly defective.

There are several cases in which the relief of lattice misfit does not destroy the coherency of epitaxy. The most common of these are rotated heteroepitaxy, in which there is a realignment of crystal axes (such as the growth of Ti on Ta); and strain relief by asymmetric coherent tilt boundaries (“tilted” heteroepitaxy), in which the epilayer nucleates and grows at an tilt angle \mathbf{q} , since the strain is correspondingly reduced by $\cos(\mathbf{q})$ [17],[18]. There are also more exotic mechanisms. For example, in the recently-discovered “internal facetting” model for strain relief at metal interfaces with square symmetry, Cu grows coherently on Ni(100) by generating internal (111) facets [19].

The principal difficulty with large lattice mismatch concerns the generation of misfit dislocations. The strain energy grows with increasing thickness of a pseudomorphically-strained film and eventually exceeds the energy barrier for dislocation formation. For cases of extreme lattice mismatch, such as the Ti/RE system, a high dislocation density greatly exceeds the forces which preserve the orientational relationship. The epitaxy is destroyed or, in the best case, the epilayer is driven into a different epitaxial orientation

which better accommodates the mismatch.

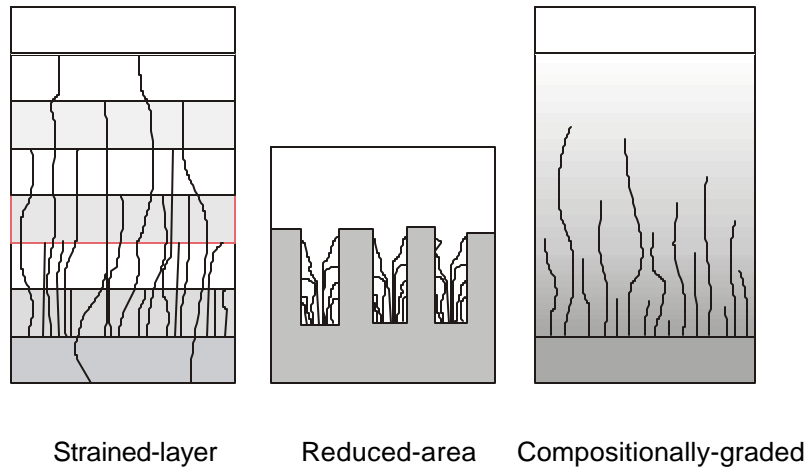


Figure 3.3. Schematic of three common experimental approaches to overcoming lattice mismatch in heteroepitaxial systems, though in general these have greater relevance to semiconductor systems (see text). The latter technique, compositionally-graded epitaxy, is adopted in the present work.

There are several approaches to overcoming lattice mismatch. These have been applied most extensively to semiconductor systems, in which the constituent epilayers have too large a mismatch and the reduction or elimination of threading dislocations is critical to electronic device performance. A common technique is strained-layer epitaxy, in which the crossover from substrate to epilayer is not made in a single step but rather in a series of alternating thin layers with thicknesses near the critical thickness for dislocation nucleation; this is shown in Figure 3.3 [20],[21],[22]. In semiconductors the Peierl's barrier for dislocation motion is large so that significant strain energy may be stored in each metastable layer; multiple layers thus provide multiple interfaces which can trap dislocations [6]. For example, semiconductor layers of thicknesses of tens of nanometers can accommodate strains of several atomic percent [23]. For this reason, application of this technique in metals is generally not possible. The Peierl's barrier is much lower, and metal overlayers relax to near-bulk structure in much thinner films than semiconductors.

Another technique is reduced-area epitaxy [24]. As shown in Figure 3.3, a reduced growth area is employed by using patterned substrates. The reduction in sample area

increases the likelihood that dislocations can reach the edge of the patterned area, where they can be trapped. Reduced area epitaxy is most effective when combined with strained-layer or composition-graded techniques [24].

The technique used in this thesis is composition-graded epitaxy, in which the composition of the bilayer is gradually changed from that of the substrate to that of the epilayer by codeposition of the constituent materials [25],[26],[27],[28],[29]. This technique is feasible for cases in which two layers are miscible and thus do not segregate during growth. Composition grading and its effects on dislocation nucleation has been studied in detail by Tersoff [27]. Dislocations in composition-graded systems are subject to weaker pinning and greater force than in uniform films. If the composition profile is chosen appropriately, the density of dislocations may be sufficient to exactly cancel the lattice mismatch up to a certain distance from the interface.

3.2 M-plane Sapphire Substrates

Sapphire (α -Al₂O₃), the second-hardest naturally-occurring mineral, is widely used as a substrate for heteroepitaxy in thin film applications. It is rhombohedral with space group $R\bar{3}c$, but it is usually indexed with a hexagonal structural unit cell ($a=4.7589$ Å, $c=12.991$ Å) containing 18 O²⁻ and 12 Al³⁺ ions [30]. This has led to confusion over the indexing of allowed x-ray reflections. The structural cell is triply primitive and has c-axis glide symmetry, hence the allowed reflections satisfy the following criteria: $-h+k+l=3n$, (hkl) ; $l=3n$, $hh\bar{2}hl$; $h+l=3n$, $l=2n$, $(h\bar{h}0l)$; and $l=6n$, $(000l)$ [31]. Sapphire substrates are grown by several methods, including the standard Czochralski method as well as submerged-crystal heat exchange methods. Wafers are cut from the resulting boules or plates, and then lapped and mechanically- and chemically-polished to obtain high-quality “epi-ready” surfaces. To date, there has been no systematic study of the way crystal quality depends on the production method. Substrates are commercially available in the following orientations, shown in Figure 3.4: A-plane $(11\bar{2}0)$, M-plane $(10\bar{1}0)$, R-plane $(1\bar{1}02)$, and C-plane (0001) ; occasionally, N-plane $(11\bar{2}3)$ sapphire has been available.

sapphire, showing the naturally-occurring crystal faces.

Due to sample charging effects below about 600 °C, in situ RHEED could not be used for surface characterization. Atomic force microscopy (AFM) was used to characterize sapphire which had been subjected to different in-vacuum and ex-situ annealing cycles. The results of these AFM measurements appear in Figure 3.5. The surface quality improves with increasing annealing temperature until about 1000 °C, above which steps are exposed and the surface roughens. Annealing of sapphire in oxygen at 1400 °C, which produces atomically-smooth surfaces for sapphire of other orientations, resulted in the formation of extremely long and well defined facets. This has been observed independently and reported [37]. The $(10\bar{1}0)$ surface is energetically less favorable than the faceted surfaces which develop, of which $(1\bar{1}02)$ is the surface of lowest unrelaxed energy for sapphire [37],[40],[41].

The improvement in surface quality with increasing annealing temperature is confirmed in a related study by the author in collaboration with Z. Wang, in which the surface chemistry of A-plane sapphire was measured by x-ray photoelectron spectroscopy (XPS). A sapphire sample was annealed for various periods in vacuum and, after each anneal, transferred to the XPS station in the EpiCenter for acquisition of Cu(K) photoelectron spectra. These spectra, shown in Figure 3.6, present clear evidence of a C signal after annealing at 800 °C whereas, after annealing at 1100 °C, no evidence of C can be seen. In the future it may be of interest to repeat this measurement with M-plane sapphire, to correlate the removal of surface contaminants with changes in surface morphology.

The quality of bcc Ta(211) grown on each of these substrates was also investigated in situ by RHEED. RHEED images of Ta grown on sapphire annealed in vacuum at 1100 °C are unusually dim. The strong shift of specular intensity into the diffuse background indicates a loss of long-range coherence. These results establish that brief vacuum annealing at 1000 °C results in Ta growth of optimal quality.

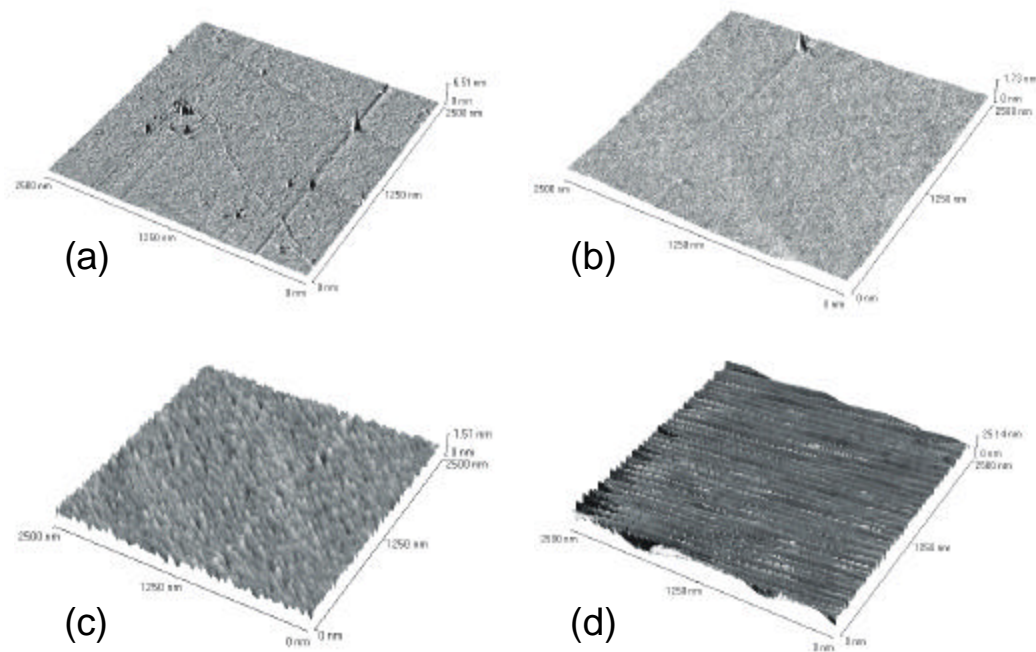


Figure 3.5. Atomic force micrographs of Mplane sapphire after different cleaning/annealing protocols. (a) Sapphire after organic cleaning but before vacuum annealing. (b) Sapphire after vacuum annealing at 1000 °C and (c) 1100 °C. (d) Sapphire after oxygen annealing at 1400 °C for 24 hrs. The apparent line defects in (a) and (b) are an artifact of the AFM leveling process.

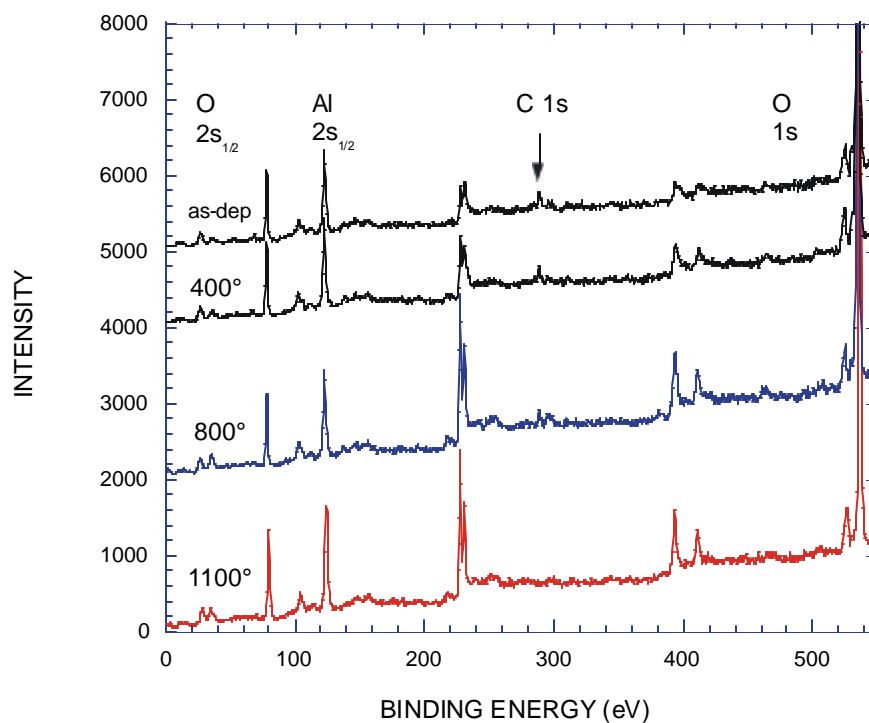


Figure 3.6. XPS photoelectron spectra of a sapphire wafer after different annealing protocols. Observe that evidence of C persists until annealing at the highest temperature.

Finally, a novel feature encountered in this research is evidence of macroscopic basal-plane slip in M-plane sapphire, which sometimes occurs during the growth of a thin film. Upon removal of a sample from vacuum, a few (usually between one and three) ultrafine streaks completely crossing the substrate can be seen with the unaided eye. These streaks propagate parallel to the $[0001]$ direction in sapphire. The crystallographic slip elements for sapphire comprise the $\{0001\}$ slip planes, and the $[11\bar{2}0]$ slip direction. Furthermore, creep by basal plane slip has been observed in sapphire under tensile loading at temperatures as low as 900 °C [42]. Such evidence of slip was not previously reported in samples which were secured by wires to sample holders [32],[43]. In the present work, however, the sapphire substrates are rigidly bonded to the Mo sample holder by high-temperature ceramic adhesive, and also maintained at high temperature for longer periods. It is possible that this slip is caused by stresses induced by differential thermal contraction between the Mo sample holder, the ceramic adhesive, and the substrate. Interestingly, the slip lines provide a convenient means for orienting the thin film after growth.

3.3 Tantalum

The first step in the growth of b-axis-oriented rare earths is to grow a bcc metal in the (211) orientation on optimally pretreated M-plane sapphire, according to the prescription of Huang and Flynn [43]. Both Ta and Nb were tried as potential buffer layers for the growth of Ti, but the highest-quality Ti was nucleated on Ta and subsequent work with Nb was abandoned. This is consistent both with the findings of Huang [43] and with the earlier observation by Du [32] that these two metals possess different bulk deformation properties. In particular, Nb(211) thin films contain substantial twinning along the in-plane $[\bar{1}11]$ axis [44].

Ta is a Group VB metal, crystallizing as bcc with space group $Im\bar{3}m$ and lattice parameter $a=3.303\text{\AA}$. The growth of bcc metals in the (211) orientation on M-plane $\alpha\text{-Al}_2\text{O}_3$ was first reported by Durbin and Flynn [2],[45]. It has the well-known epitaxial orientation

$$\text{Ta}[\bar{1}11] // \text{Al}_2\text{O}_3[0001],$$

$$\text{Ta}[0\bar{1}1] // \text{Al}_2\text{O}_3[11\bar{2}0]),$$

as shown in Figure 3.7. The two-dimensional surface symmetries suggest that two variants of bcc metals are expected on sapphire, although only one variant is actually observed. This is explained by the complicated rhombohedral sapphire structure. As reported in Reference [46] and shown in Figure 3.8, the initial bcc layer tries to occupy positions of the nearly hexagonal Al^{3+} sublattice, which has unique stacking sense and thus breaks the two-fold surface symmetry.

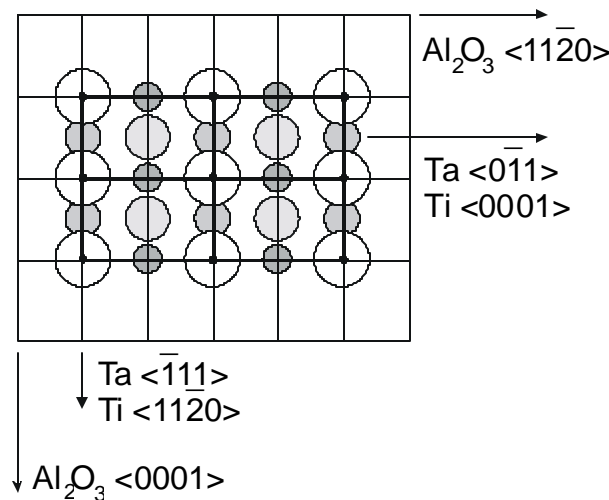


Figure 3.7. The orientational relationship of the epitaxial layers which compose b-axis-oriented rare earth thin films. The balls represent successive layers in the ABCDE... stacking sequence of Ta(211). Note that the sapphire and Ti/RE surface nets are rotated by 90° with respect to each other.

Growth

Ta was obtained by electron beam evaporation of high purity Ta at growth rates between 0.01 to 0.05 nm/s. The vacuum chamber pressure was typically 7×10^{-11} torr prior to growth, and it rose to 5×10^{-9} torr during growth due to the release of H_2 . The low base pressure is partly due to the strong gettering by evaporated Ta [47],[48]. The optimal growth temperature of bcc buffer layers such as Ta(110) and Nb(110) has been reported at 900 °C and this substrate temperature was initially used. RHEED measurements that

revealed these surfaces exhibited facetting and strong 1D disorder, as shown in Figure 3.11. The quality of Ti grown subsequently depended strongly on the Ta morphology observed by RHEED, so it was necessary to optimize the quality of Ta(211).

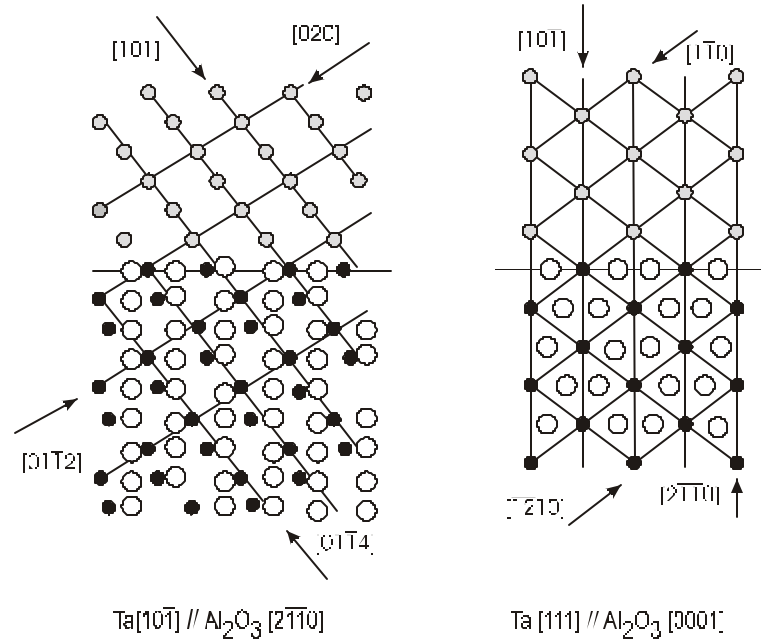


Figure 3.8. A detailed view of the Ta(211)//Al₂O₃ interface, showing that the Ta layer continues the Al sublattice. The dark balls and light balls are Al and O anions and cations, respectively.

The growth temperature was carefully refined using optimally pretreated sapphire. RHEED measurements showed that for Ta growth temperatures between 750 °C to 790 °C, or when the growth pressure was not optimal, a well-ordered surface with a 2x8 reconstruction resulted. From 790 °C to about 850 °C, the reconstruction is 3x7, as shown in Figure 3.9.

For growth temperature above about 850 °C, surface facets develop and the surface exhibits strong 1D disorder, as seen in the curved RHEED pattern shown in Figure 3.10. For the case of a two-dimensional surface with complete one-dimensional disorder in one direction (usually the close-packed direction, as in this case), the corresponding reciprocal space broadens into a series of sheets, narrow in the direction of order but sheet-like in the direction of disorder. The intersection of these reciprocal lattice sheets with the Laue circle is set of curved streaks, as observed. The RHEED pattern measured along the $[\bar{1}11]$

azimuth was first observed by R. Du. As discussed in Reference [2], Ta has {211} twinning planes and [111] easy shear directions, and therefore this 1D disorder is consistent with bulk deformation properties.

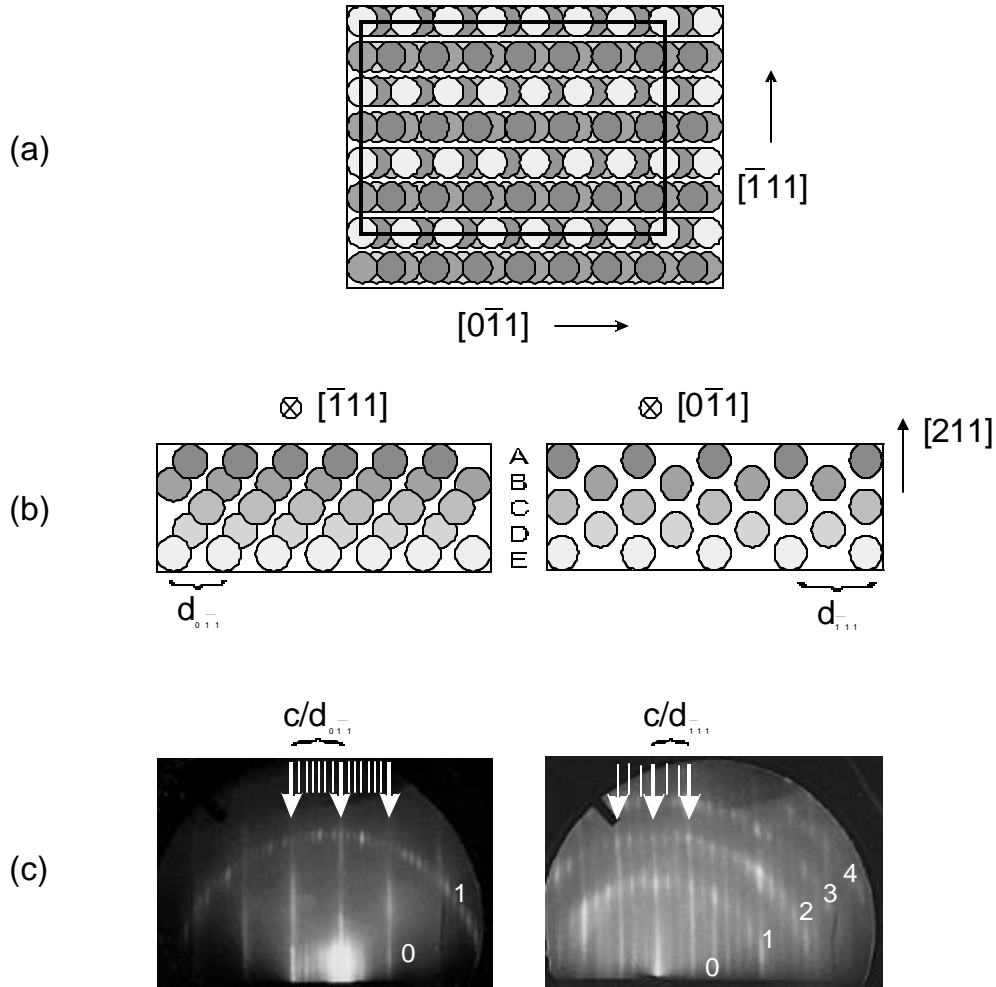


Figure 3.9. (a) The Ta(211) surface. The balls denote successive layers in the ABCDE... stacking sequence. The rectangle is the unit cell of the observed surface reconstruction. It is approximately coincident with the misfit dislocation network measured by TEM. (b) Elevation views along two axes. (c) RHEED images along the high symmetry directions, showing the 3x7 reconstruction characteristic of optimally-grown Ta. For optimal Ta, many orders of Laue circles can be seen.

AFM measurements performed after growth (see Figure 3.22) also indicate that the smoothest surfaces are obtained at $T_g=790^\circ\text{C}$. As with the optimization of sapphire discussed above, the refinement of Ta was made more complicated by the need to verify each time the quality of the subsequent growth of Ti. The highest-quality Ti was found to

nucleate on the highest-quality Ta, confirming that the best substrates yield the best epilayers.

Microstructure

X-ray diffraction (XRD) studies of Ta were less useful for optimizing film quality, since all samples exhibited the same longitudinal and transverse linewidths. This indicates that the long-range orientational order probed by high-angle x-ray diffraction is less sensitive to growth temperature than is the short-range surface order.

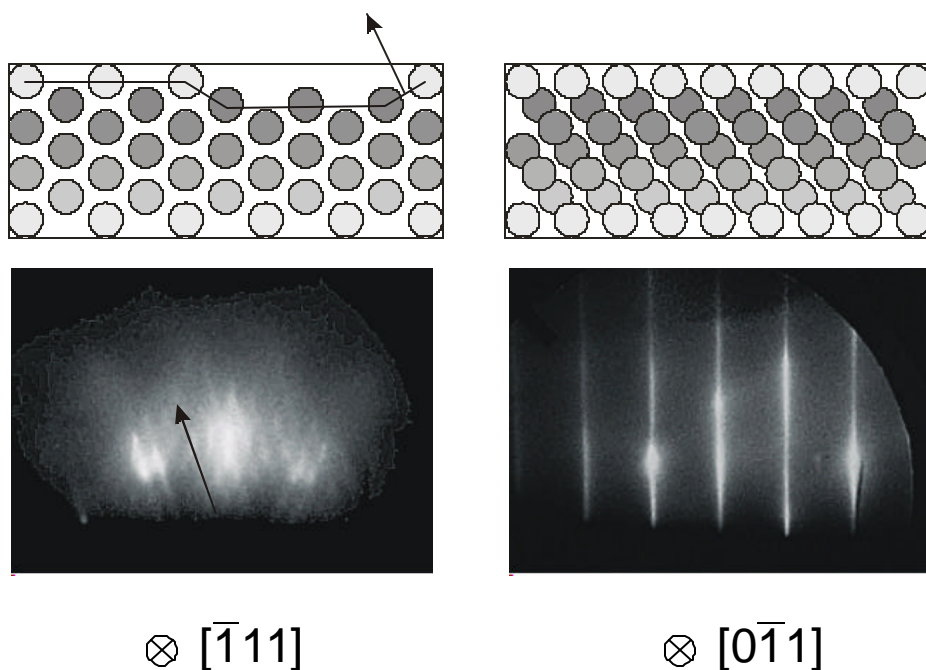


Figure 3.10. RHEED patterns from a Ta(211) surface grown above 850 °C which exhibits facetting along one direction. (Left) The RHEED pattern is parallel to the facet surface direction, giving rise to the inclined diffraction streaks. (Right) The faceted surface is rough, so modulations of intensity can be seen along the streaks.

Anisotropic in-plane linewidths of about 0.3°. Owing to the high scattering angle and the low intensity, it was not possible to measure the (422) reflection using the fixed-tube DMAX diffractometer. This reflection was measured, however, in collaboration with I.

Robinson at the X16A beamline of the NSLS and it was shown that the (211) and (422) reflections exhibit equal angular width, so that the broadening is due to crystal mosaic rather than in-plane domain size limitations.

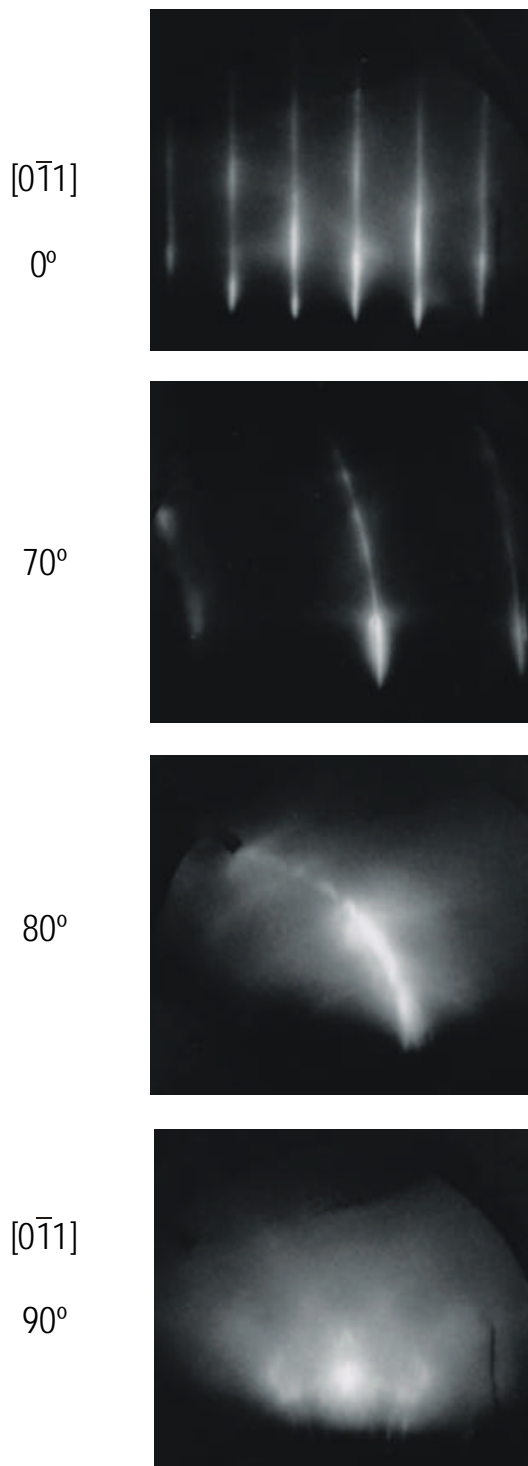


Figure 3.11. Ta(211) grown above 850 °C exhibits strong 1D disorder, as shown here. Random

structural disorder in the surface atomic positions gives rise to sheets of scattering intensity in reciprocal space. The observed pattern is arcs of intersection of these sheets with the Laue circle.

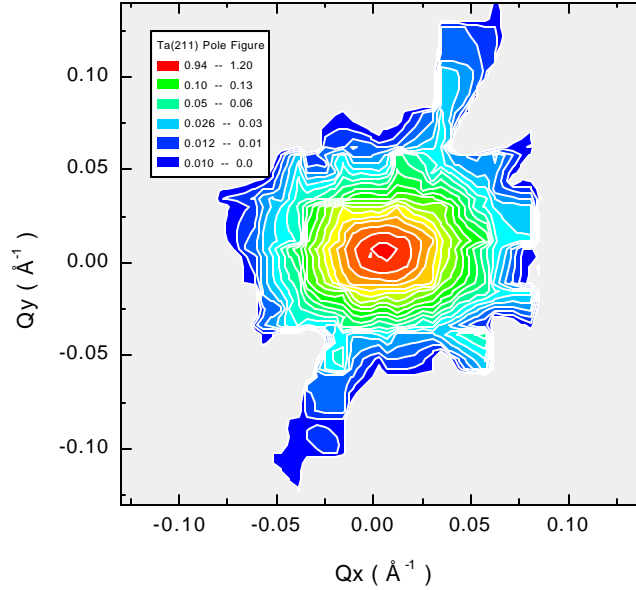


Figure 3.12. X-ray diffraction pole figure for the Ta(211) peak, showing the anisotropy of in-plane structural order. Q_x and Q_y are parallel to Ta[011] and Ta[111], respectively. The pronounced feature inclined at about 45° is an artifact of a long scan in this direction.

The bcc/sapphire interface has been studied in detail for the case of Nb using high-resolution cross-section transmission electron microscopy (HRTEM) by the group of M. Rühle at the Max-Planck-Institut für Metallforschung in Stuttgart, using samples grown by the author [46]. As reported by this group, this heteroepitaxial interface is semi-coherent and the misfit is accommodated by a two-dimensional network of dislocations. It is likely that a similar anisotropic dislocation network in Ta gives rise to the observed anisotropic mosaic disorder. It is not known if this is related to the 3×7 reconstruction observed by reflection high-energy electron diffraction (RHEED) subsequent to growth as discussed above. Work in progress by Sweich and Flynn using low-energy electron microscopy is further elucidating the nature of the bcc/sapphire interface.

Possible Oxygen Contamination

An interesting observation concerns the possible oxygen contamination of Ta. RBS spectra of Ta on sapphire show Ta peaks with less coverage than one would predict for pure Ta. These data are not adequately fit unless the Ta film is assumed to contain a substantial fraction of oxygen, often as much as 50% [49]. This behavior has not been noticed for Nb on sapphire, even for Nb films annealed at 1500 °C. It is well-known that Ta reacts with polycrystalline alumina at high temperature, and oxygen-contaminated Ta grown on sapphire has been reported in earlier studies [50],[51].

It is interesting to speculate whether an oxygen-rich surface may affect the observed preference for high-quality Ti to nucleate on a Ta surface rather than a Nb surface. It is known that oxygen on the surface of Ti occupies the Ti interstices and passivates the Ti against further oxidation [52]. This is corroborated by an AFM study of Ti surfaces by the author, first after immediate exposure to air and subsequently after one month in air, which revealed remarkably little degradation of the observed Ti surface morphology. It is currently not known if oxygen at the surface of Ta may act as a benevolent surface surfactant or annealing agent [53].

3.4 Titanium

Titanium is a group IVA metal, crystallizing in the hcp orientation with space group $P6_3/mmc$ and a melting temperature of 1660 °C. The nucleation of hcp Ti(1 $\bar{1}$ 00) on bcc Ta(211) is the hcp-bcc variant of the Kurdjumov-Sachs orientational relationship, in which the close-packed crystallographic directions are parallel, as shown in Figure 3.8 [54].

$$\text{Ti}[11\bar{2}0] // \text{Ta}[\bar{1}11] // \text{Al}_2\text{O}_3[0001],$$

$$\text{Ti}[0001] // \text{Ta}[0\bar{1}1] // \text{Al}_2\text{O}_3[11\bar{2}0];$$

that is, the hexagonal a- and c-axes of Ti and sapphire are misoriented by 90°.

Growth

The initial studies of Ti growth on Ta were conducted on M-plane sapphire obtained from Union Carbide (Crystal Products Division), with a surface miscut angle of 1.5°. M-plane

sapphire from Crystal Systems with a miscut less than 0.5° was later obtained and was used for all subsequent work.

The pre-annealing of sapphire and growth of Ta proceeded in one MBE system, and the samples were subsequently cooled to room temperature and transferred in UHV (5×10^{-10} torr) to a second system for the deposition of subsequent materials. The growth of 50 nm of Ti via electron-beam evaporation at fluxes between 0.01 and 0.05 nm/s was studied for substrate temperatures up to $T_g = 700^\circ\text{C}$. The RHEED streaks sharpen with increasing temperature, indicating an improvement in the in-plane structural coherence.

Both RHEED and XRD measurements performed after growth indicate that single crystal Ti ($1\bar{1}00$) is obtained for growth temperatures below 700°C . However, a growth temperature of 700°C resulted in Ti ($11\bar{2}0$) [55]. Information about the structural properties of Ti ($11\bar{2}0$) grown in this manner were not pursued, since this crystallographic orientation is not an objective for the growth of b-axis-oriented rare earths. In earlier work, Huang found that other orientations of Ti could be nucleated on Al_2O_3 ($10\bar{1}0$), depending on temperature and the magnitude and direction of the sapphire miscut [43]. The present research makes clear that a complete elucidation of the nature of Ti growth on Ta is complicated by the many factors associated with the growth of these three-layer Ti/Ta/ Al_2O_3 structures, not only sapphire miscut but also sapphire pre-growth treatment and refinement of Ta(211) buffer layer quality.

Computer/CCD acquisition of RHEED intensity during growth provided information about the surface morphology and growth mode. The first few Ti monolayers are pseudomorphically-strained to the Ta, but shortly thereafter a distinct series of surface facets and reconstructions appear, as shown in Figure 3.13. The sudden change of the diffraction pattern and the loss of specular intensity after 10 Å suggests the growth mode is of the Stranski-Krastanov type. A similar initial growth mode occurs for Lu on Zr, discussed below. After about 50 Å a facet-free, unreconstructed surface is stabilized, and the RHEED intensity exhibits oscillations whose period corresponds to the deposition rate and with no evidence of damping during the time required to complete the layer. These

data are presented in Figure 3.14. This indicates the transition to a stable, layer-by-layer growth mode.

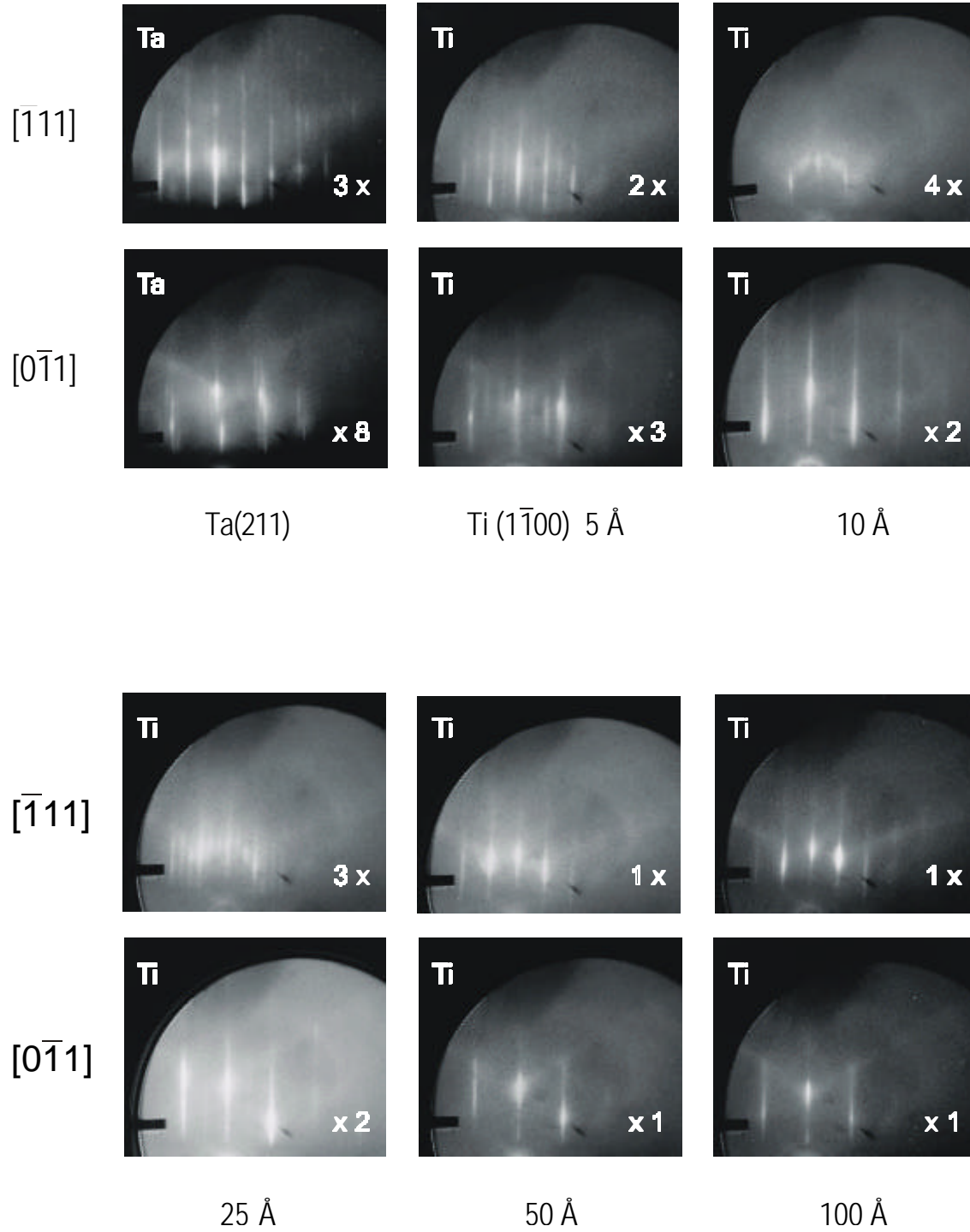


Figure 3.13. RHEED images during the initial stages of Ti(1100) epitaxy on Ta(211). The sudden change in the diffraction pattern at 10 Å may indicate a critical thickness for a Stranski-Krastanov

growth mode. After about 50 Å a smooth, unreconstructed surface of Ti is stabilized. The symbols in the lower right label the surface reconstruction along the given azimuth.

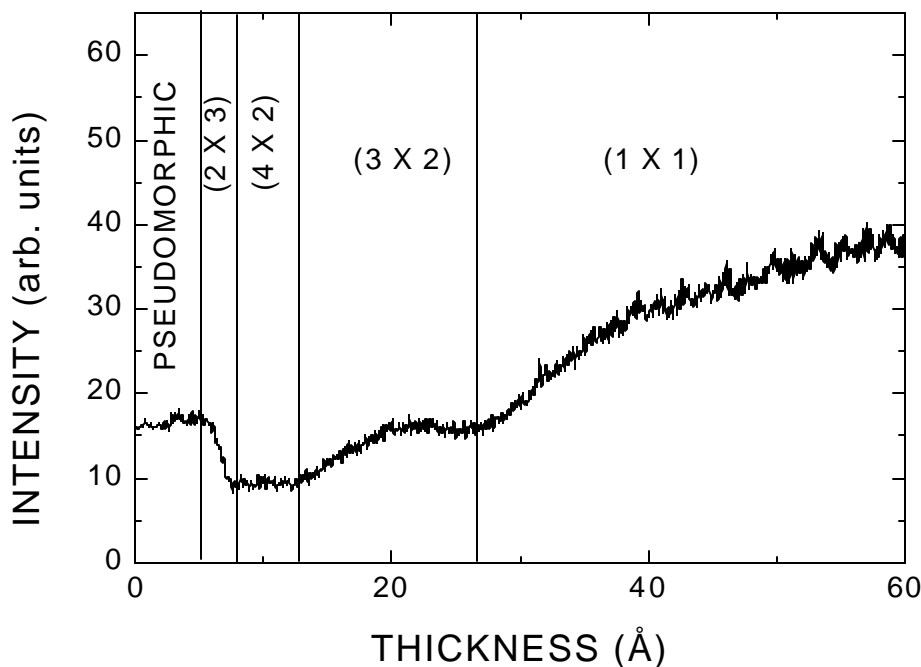


Figure 3.14. The RHEED specular intensity recorded during the growth of b-axis-oriented Ti on Ta(211) under optimal conditions. The jumps in intensity correspond to the development of surface reconstructions. After a thickness of about 50 Å, oscillations of intensity appear and these have a period equal to the time required to complete a monolayer. The high-frequency oscillations are from interference by the electron beam evaporation system.

Microstructure

AFM was performed on the Ti surfaces after growth with the results shown later in Figure 3.22. Ti is reactive but on exposure to air its surface develops a self-passivating interstitial oxide. It is likely that the surface morphology observed ex situ by AFM does not differ from the morphology of the as-grown surfaces in vacuum [56]. Moreover, the morphology persisted without degradation in air for up to one month, after which it degraded slightly. For the lowest growth temperatures, the restricted adatom mobility limits the formation of mesostructure and thus the films are grainy but flat. Above 400 °C, a stepped morphology is observed and this persists for higher temperatures. This stepped microstructure is consistent with the measured deviation (about 1.5 degrees for these samples) of the miscut

sapphire surface from the true $(10\bar{1}0)$ direction.

Surface roughness can be quantified in several ways. Quantities such as the RMS roughness are frequently not useful, as discussed in Chapter 2. In what follows, these data are quantitatively reduced by employing a lake-filling model. A computer algorithm is applied to assess the perimeter of contiguous regions of surface below a given height threshold, and then to compute the ratio of the perimeter (p) of these regions to their area (A). As Figure 3.15 shows, a surface with frequent height deviations above and below the mean (small, irregular lakes) possesses a larger p/A ratio than a smoothly-varying surface with large contiguous regions above and below the height threshold. Interestingly, the in-plane mosaïcities obtained by XRD are correlated with the surface roughness, as shown in Figure 3.15. The best in-plane coherence, obtained at about 550 °C, coincides with the smoothest surfaces. Since the crystal mosaic measured by XRD depends on the correlation function which describes structural disorder in the crystal, it not surprising to find that the surface and bulk roughnesses are similar [57].

Finally, the anisotropic microstructure apparent both in AFM measurements (Figure 3.15) and XRD measurements (Figure 3.21) is addressed. The anisotropy agrees with the anisotropic Ti/Ta lattice mismatch; that is, the surface morphology is elongated and the mosaïcity is reduced in the direction of least misfit. This is most probably the result of a lower density of dislocations with this direction.

3.5 Titanium/Zirconium Composition-Graded Epitaxy

The hcp b-axis orientation was established by the growth and optimization of high-quality thin films of Ti $(1\bar{1}00)$. However, Ti retains nearly 20% lattice mismatch with the rare earths. With few exceptions, typically involving epitaxy of materials in their low-energy “habit” orientations, such as bcc(110) and hcp(0001), lattice mismatches larger than about 2% between substrate and epilayer present an obstacle which often prevents the successful growth and nucleation of the epilayer.

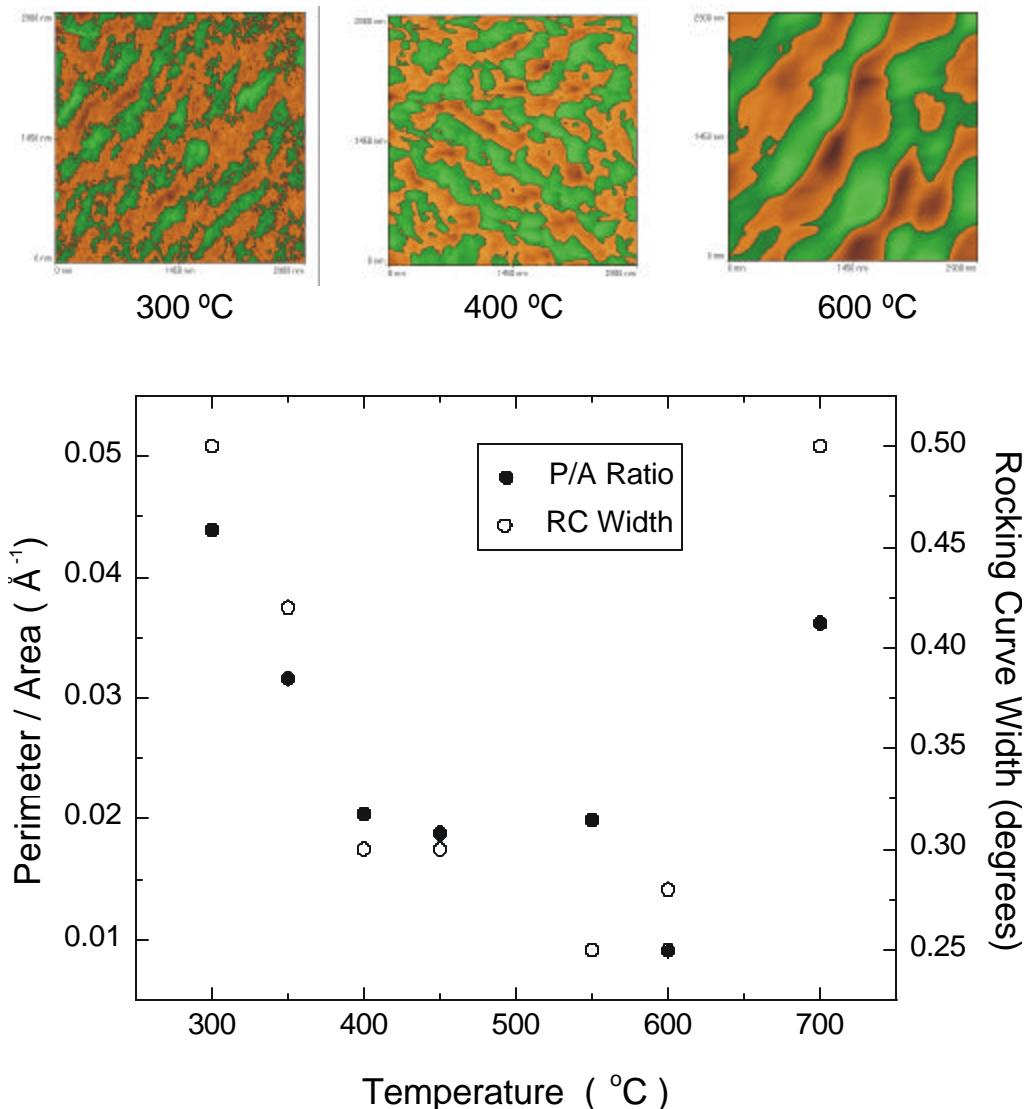


Figure 3.15. The results of a lake-filling roughness analysis of AFM data for Ti grown on Ta(211) at different temperatures. (Top) The lakes are superimposed in false color on the AFM images. The sequence of lakes show a pronounced smoothing with increasing growth temperature. (Bottom) The ratio of lake perimeter/area vs. growth temperature, showing a correlation with the transverse XRD linewidth.

An intermediate buffer layer of Zr was used to partially mitigate this problem. Zr is also a group IVA metal, crystallizing in the hcp orientation with space group $P6_3/mmc$, and has a melting temperature of 1852 °C.

To overcome the lattice mismatch a composition-grading scheme was used. There is good reason for technique to be more successful than the other procedures discussed in Section 3.1. First, the surface free energies of Ti and Zr are nearly equal at 2.570 J/m² and

2.790 J/m², respectively, hence wetting as a strong driving force for pseudomorphic nucleation of Zr on Ti below a critical thickness does not exist [58]. Second, since the optimal growth temperature of Ti is fairly high, and since Zr and Ti both possess atypically large diffusion coefficients (possibly enhanced in the $[1\bar{1}00]$ direction [59]), interfacial intermixing may be difficult to control. Third, Zr is completely miscible with Ti [60], therefore no segregation during growth is expected.

Growth

It was necessary to control the growth parameters manually during Ti/Zr grading, a process requiring about two hours. This was accomplished in the following manner. First, a stable Ti flux of about 0.02 nm/s was established and a 25 nm thick Ti ($1\bar{1}00$) film was nucleated and grown on Ta. (A high-quality, unreconstructed Ti surface was stabilized after about 5 nm, as described above.) Next, a Zr flux was established in parallel with the Ti but a factor of 100 smaller. The Zr flux was slowly increased at five-minute intervals, helped by the tendency of the electron-beam power supply to drift and supply increasing power over time without operator intervention, thus smoothing the process of grading. After the Zr rate reached a level of about 0.02 nm/s, the Ti flux was slowly reduced and finally eliminated, with the evaporation of Zr continued uninterrupted for a further 50 nm. A typical grading profile is shown in Figure 3.16.

Considerable effort was spent to improve film quality, including adjusting the grading rate and the substrate temperature during grading. Optimal film quality was achieved by lowering the growth temperature from 550 °C to 450 °C during the grading process. This is confirmation of earlier work by Huang, in which a temperature of 450 °C was reported as the optimal growth temperature for Zr [43]. The melting temperature of 1852 °C for Zr is higher than that of Ti, 1660 °C, so a lower optimal growth temperature must be due to the unusually large diffusion coefficient of Zr [61].

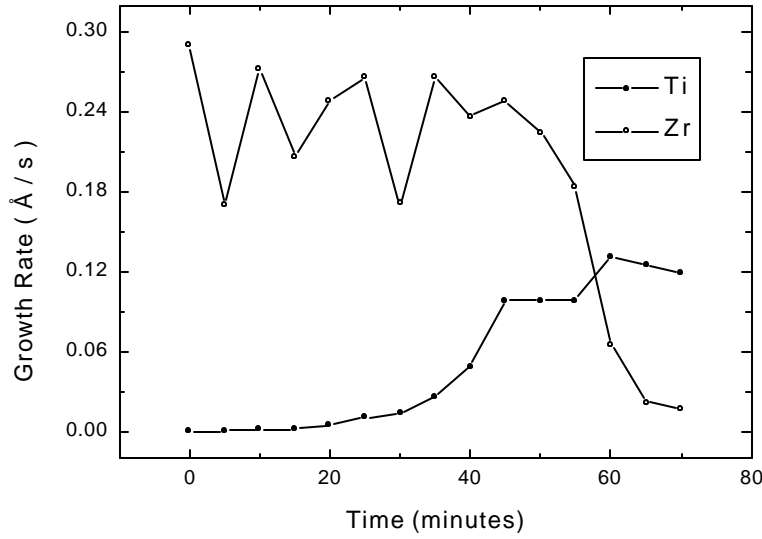


Figure 3.16. The recorded Ti and Zr fluxes during composition grading, measured with a calibrated RGA. The actual fluxes were continually adjusted so that the average rate is more stable than shown here.

Experimental Details

For completeness, three further experimental details are addressed. These are needed in attempts to reproduce this work successfully.

Oxygen contamination of Zr source material. The Zr flux prior to lengthy outgassing contains a significant fraction of ZrO as a parasitic and deleterious contaminant, often as high as 10% according to the levels detected by the RGA. ZrO₂ is the stable oxide in air but studies and calculations of Zr oxide decomposition reveal that ZrO will be present in the highest abundance during evaporation with ZrO : ZrO₂ : Zr = 4 : 1 : 0.7 [62],[63],[64]. It is therefore essential to outgas of the Zr source material before growth in order to reduce ZrO to a level below 1%, which was found to be acceptable for the reproducible growth of b-axis-oriented Zr.

Effect of Zr on RGA. It is known [65] that Zr strongly reduces the Richardson coefficient A which governs the rate of thermionic electron emission J from a filament with workfunction f , in the equation $J = AT^2 \exp[-f/k_B T]$. Since the residual gas analyzer adjusts its filament current to stabilize a constant emission current, Zr deposition on the filament

reduces the filament current and further increases more Zr deposition on the filament, a positive feedback process. This effect was eliminated by operating the RGA at a higher emission current of 34 mA rather than the normal 2 mA. After growth, the emission current was briefly raised to about 5 mA, resulting in a sudden increase then diminution of the Zr level as residual Zr was flashed off, thereby “cleaning” the filament of accreted Zr deposition.

Correct RGA resolution adjustment. Since Zr (91.22 amu) has a wide isotope distribution and almost twice the atomic mass of Ti (47.90 amu), the doubly-charged Zr peak nearly overlaps with the Ti peak as detected by the RGA. This makes an accurate measurement of the ratio of these species difficult. Adjustments of the RGA resolution alone affect the sensitivity, and thus it is necessary to adjust both the RGA resolution and the gain properly, through the electron multiplier high voltage bias, so that these overlapping peaks can be resolved while still maintaining the large dynamic range required to properly monitor the grading process.

3.6 Zirconium

After grading Zr into Ti the growth of pure Zr was continued uninterrupted at 450 °C up to a thickness of 50 nm. The chamber pressure during growth was consistently below 1×10^{-9} torr, due to strong gettering by Ti and Zr [48].

Post-growth Annealing

A key step for the nucleation and growth of high-quality rare earths on Zr is a post-growth annealing of the Zr layer. The quality of the Zr surface is greatly improved by annealing at 550 °C for one hour prior to the deposition of the rare earths. Figure 3.17 shows the RHEED images of Zr taken after growth and after annealing for one hour at 550 °C. This annealing temperature is the maximum limit; the Zr RHEED pattern immediately disappears for higher temperatures, suggesting complete loss of surface order [55].

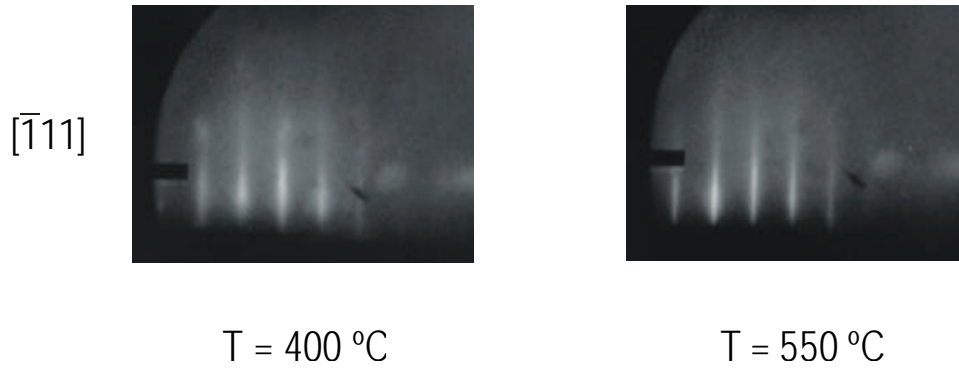


Figure 3.17. (Left) The RHEED image of a Zr surface at 450 °C following growth under optimal conditions. (Right) The same Zr surface after annealing for one hour at 550 °C.

Microstructure

In situ RHEED shows the Zr to be a single-crystal and well-ordered after annealing. X-ray diffraction measurements on the films indicate anisotropic in-plane linewidths of between 0.6° and 1° , evidently due to crystal mosaic. Since two materials with a misfit of 10% cannot be accommodated by strain, the Ti/Zr misfit must be relieved by dislocations or defects, thereby leading to increased mosaic widths. A reciprocal space map of scattering intensity along K_\perp and K_\parallel for the region between the Ti and Zr Bragg peaks is presented in Figure 3.18. The in-plane linewidth increases about halfway between Ti and Zr, suggesting that lattice misfit is accommodated without reduction of coherence until the grading reaches a 50% composition.

Anisotropic surface morphology is also revealed by AFM measurements (Figure 3.22). The anisotropy of the morphology is consistent with both the XRD in-plane anisotropy and the misfit anisotropy: the domains are longer along $[11\bar{2}0]$, which is the direction of least misfit. It was not possible to further improve crystal quality by varying growth conditions.

3.7 Rare Earths

After growth of the b-axis-oriented Zr buffer layer, there remains nearly 10% lattice mismatch between the Zr and the rare earths. Given the existing success in nucleating and

growing Zr on the grossly-mismatched Ti buffer layer, this suggests that a similar composition-grading scheme may be useful. The binary phase diagrams of the rare earths with Zr or Ti show a complete miscibility gap, however, so that that composition-grading will most probably fail due to segregation. Fortunately, Lu can be grown heteroepitaxially on Zr, as discussed next.

Growth

It was found that b-axis-oriented Lu can be nucleated and grown as a high-quality single crystal directly on Zr. Following post-growth Zr annealing and temperature stabilization at 550 °C, Lu was deposited at 0.001 nm/s by evaporation from a high-temperature Knudsen-type evaporation cells. This growth rate is over one order of magnitude slower than usual (0.02 to 0.05 nm/s), but the growth temperature is less than the 700 °C temperature used to nucleate c-axis-oriented rare earths on Ta or Nb buffer layers. As first elucidated by Flynn [66], there is a competition between the roughening process of adatom-adatom nucleation and the smoothing process of adatom-step nucleation; this depends on surface diffusion and the growth rate. For b-axis-oriented Lu, suppressed surface diffusion due to reduced temperature must be compensated by a reduction in growth rate.

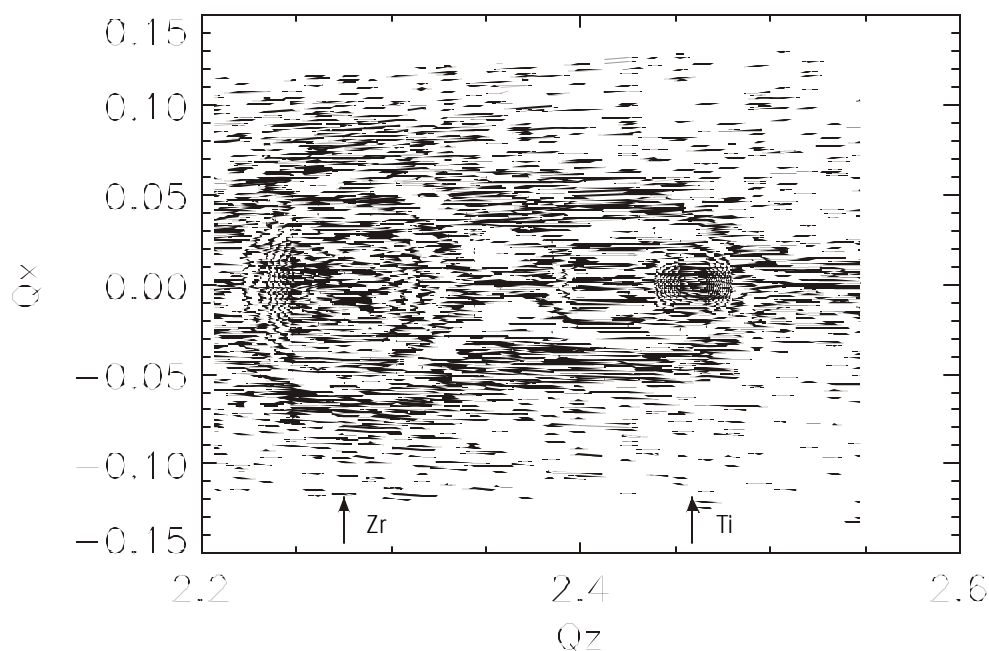


Figure 3.18. An XRD map of the region between the Ti Bragg peak (right, 2.45\AA^{-1}) and the Zr peak (left, 2.3\AA^{-1}). The increase in width along Q_x which occurs about halfway between the peaks suggests the structural quality degrades after the Zr/Ti alloy composition is about 50%.

RHEED studies of Lu growing on Zr clearly identify the Stranski-Krastanov growth mode. The data are shown in Figure 3.19. For thicknesses up to 1.8 nm, the Lu is pseudomorphic with the Zr buffer layers but with an increasing loss of long-range order, indicated by the shift of specular scattering intensity into the diffuse background. Above about 2 nm, the diffraction pattern changes to a superposition of vertical, broad streaks on a triangular network of streaks. This indicates a coexistence b-axis-oriented facets. After about 5 nm, the facet intensity diminishes and the vertical streaks which denote a single-crystal ($1\bar{1}00$) grow in intensity and sharpen with increasing film thickness. In the best sample obtained, which was a 500 Å Er film, a final Lu cap layer applied to the structure showed a 5×1 surface reconstruction, as shown in Figure 3.19.

The low growth rate must be maintained until a thickness of about 10 nm, after which RHEED measurements indicate a stable b-axis-oriented Lu surface. Subsequently, the rate can be increased gradually to 0.02 nm/s. No evidence of RHEED intensity oscillations could be observed. This indicates either that the homoepitaxial regime of Lu growth takes place by step-flow growth or, more likely, that the growing surface has developed a steady state mean structure.

The Stranski-Krastanov growth mode originates with the much lower surface free energy of the rare earths (typically 0.8 - 1.1 J/m²) compared to Zr (2.79 J/m²) or Ti (2.57 J/m²) and hence their proclivity to wet [58]. Specifically, the growing Lu epilayer can reduce the total free energy by completely covering the Zr surface, but with a strain energy which grows with increasing Lu thickness. Above a critical thickness (in this case, about 1 nm) the strain energy is sufficient to overcome the reduction in surface energy, resulting in the growth of faceted islands which accompany the introduction of misfit dislocations.

Tunably-Strained Dy

Alloys of Y and Lu were used to synthesize tunably-strained Dy. The alloys were realized experimentally by a composition-graded process: the growth of Lu on Zr was continued, and a flux of Y was gradually added and increased until the desired alloy composition was obtained. During this process, the residual gas analyzer was used to establish appropriate values of the growth rates for Lu and Y. After obtaining the flux ratio desired for a given alloy the substrate temperature was reduced to 400 °C to prevent interdiffusion. Layers of Dy 7 nm thick were then grown sandwiched between 50 nm layers of Y-Lu alloy. It was found that 5 such layers were sufficient to provide an adequate magnetic signal for detection by the SQUID magnetometers. Finally, the completed samples were capped with a small amount of Y, to inhibit oxidation upon removal from vacuum.

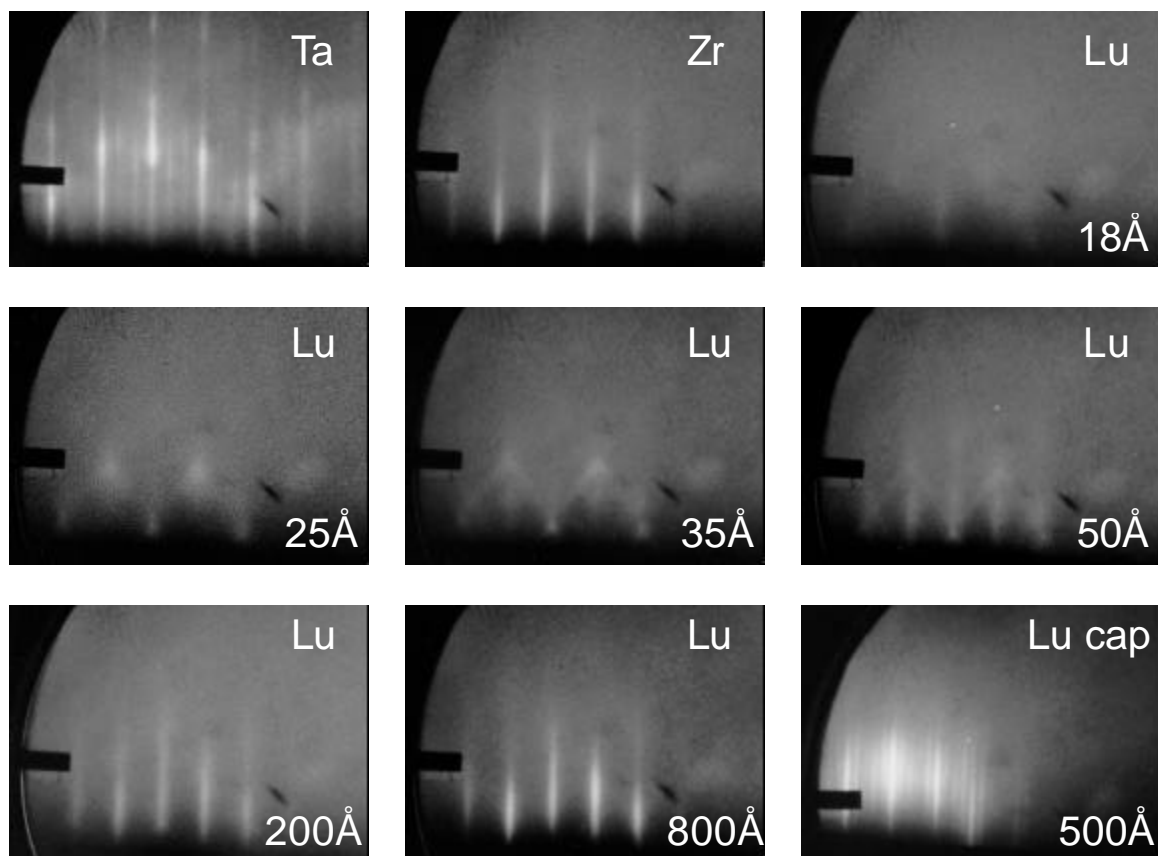


Figure 3.19. A sequence of RHEED images taken during the growth of Lu on Zr under optimal growth conditions and illustrating the Stranski-Krastanov growth mode. Before about 18 Å, the growth of Lu on Zr is pseudomorphic, with diffracted intensity gradually shifting into the diffuse background. After about 25 Å a superposition of inclined streaks and vertical streaks gradually gives way to vertical streaks only, indicating that surface becomes smoother and the facets disappear. The final image is a thin Lu cap layer taken after the growth of a 500 Å Er film; the surface exhibits a 5x1 reconstruction.

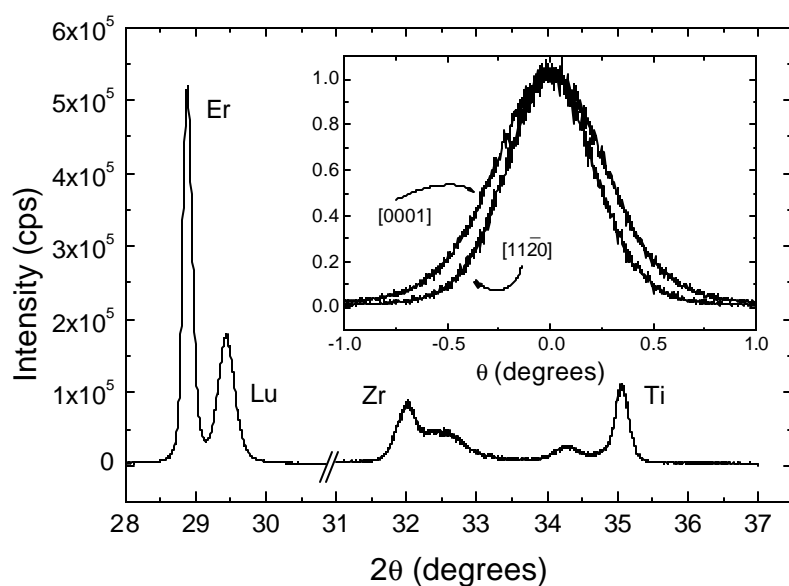


Figure 3.20. Longitudinal XRD measurement showing the b-axis-oriented rare earth Bragg peaks, as well as the Ti and Zr buffer layers (scaled by a factor of 5 for clarity). Note the small peaks which are sometimes present between Zr and Ti; it is not known if these are due to instabilities in the compositional-grading, or else due to a metastable Zr/Ti alloy. The inset shows the transverse anisotropy of the Bragg peaks.

Microstructure

Completed films were removed from vacuum and examined by atomic force microscopy and x-ray diffraction. XRD measurements reveal well-resolved out-of-plane, longitudinal lineshapes, as shown in Figure 3.20, in which line splitting due to $K\text{-}\alpha_{1,2}$ can be resolved in the thicker films. Transverse “rocking curve” measurements have typical linewidths between 0.4° and 0.7° (0.3° has been achieved for rare earths grown under optimal conditions). Higher order reflections have the same angular linewidth, confirming the roughness is mosaic disorder.

Figure 3.21 presents a summary of in-plane XRD measurements on a b-axis-oriented Er/Lu film which is typical for these thin films. Two important results are immediately apparent. First, the in-plane linewidths are anisotropic and the direction of anisotropy is consistent with the lattice mismatch between successive layers. This is true also for the

case of Ti, for which the in-plane anisotropy is rotated by 90° with respect to the others. Second, the linewidths increase from Ta to Ti to Zr but they reduce for Lu and subsequent rare earths. If the mosaicity is the conventional rotational disorder from elastic strain fields which surround dislocations [67], [68], then evidently the dislocations are trapped at the Zr/Lu interface.

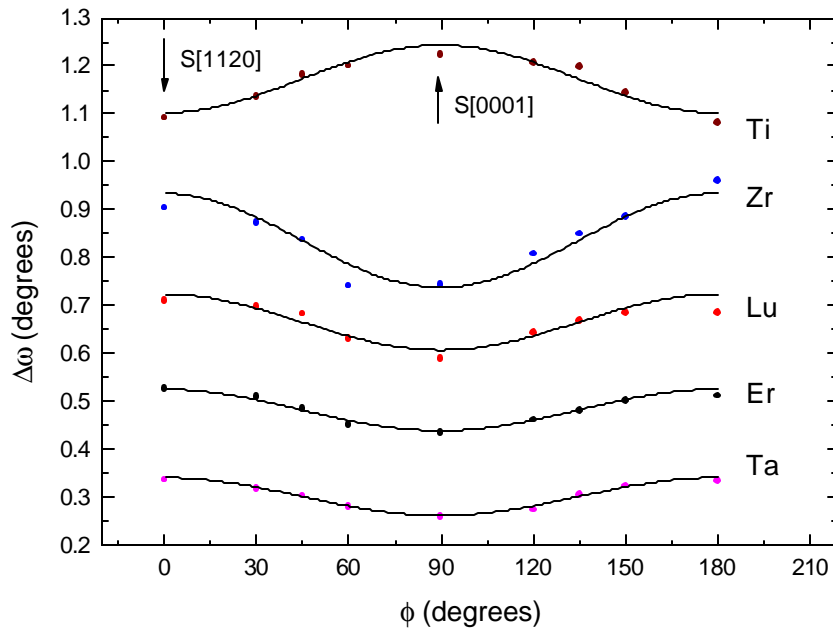


Figure 3.21. XRD measurements of the anisotropy of the transverse widths of Bragg peaks for the layers which compose the baxis-oriented samples. The 0° and 90° points are parallel to the sapphire [1120] and [0001] directions, respectively. The Ti data have been shifted by 0.8° for clarity. The Ti anisotropy is shifted by 90° with respect to that of the other samples, and the magnitude of the anisotropy actually decreases subsequent to the Zr layer.

The rare earth layers of the best samples possess in-plane XRD linewidths of about 0.3° , roughly comparable to the mosaic width of the initial Ta and Ti layers. This suggests that disorder introduced for strain relief in Ta/ Al_2O_3 limits the structural perfection of the final layers, possibly through threading defects or dislocations. Unlike the epitaxy of Ta(110) on $\alpha\text{-Al}_2\text{O}_3(11\bar{2}0)$, the Ta(211) layer has neither a two-component in-plane lineshape nor satellite reflections that correspond to coherent in-plane strain waves. Thus

epitaxy of Ta(211) has less coherence than Ta(110) on $\alpha\text{-Al}_2\text{O}_3(11\bar{2}0)$. This difference may derive from a specific pathway for bcc crystals whereby dislocations can accommodate lattice misfit by glide and cross-slip. This the subject of work by G. L. Zhou in this research group [9]. For bcc crystals, the slip plane is (110) and therefore in bcc(110) crystals the dislocations can slip almost parallel to the surface. For the present case of Ta(211), a {110} plane is not parallel to the surface; dislocations may therefore thread, giving rise to additional structural disorder which the bcc(110) system can avoid [70].

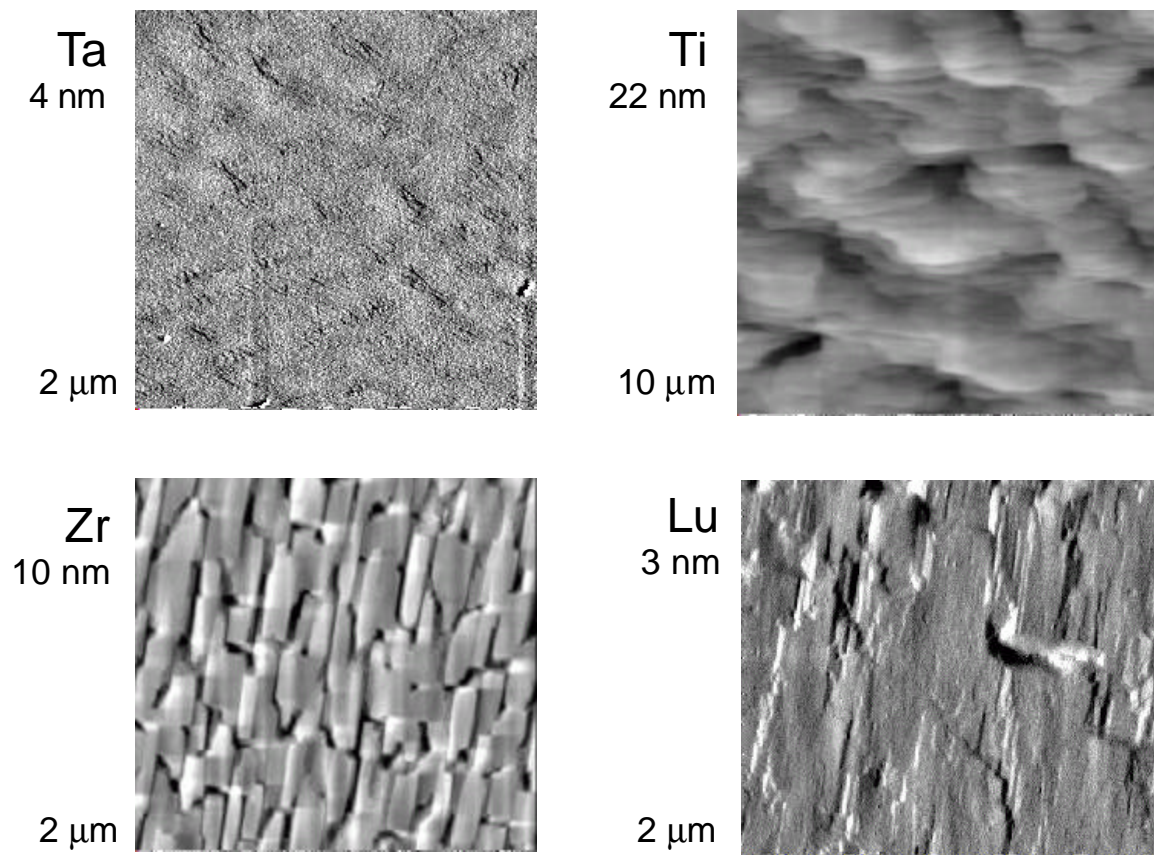


Figure 3.22. AFM images taken from the Ta, Ti, Zr, and rare earth layers which compose a b-axis-oriented rare earth sample. The sapphire [0001] direction is vertical. Two key features are that Ti exhibits anisotropy which is rotated by 90° from that observed for the subsequent materials, and that the pronounced roughness of the Zr surface evidently heals during the growth of rare earths

(1103) - oriented Rare Earths

($1\bar{1}03$)-oriented Lu was obtained when the substrate temperature was held below the

optimal value of 550 °C required for the b-axis-orientation. Further growth and microstructural studies were avoided, since this observation (though interesting) is not relevant to the goal of growing b-axis-oriented rare earths. Future work, however, may usefully exploit this new pathway for materials synthesis.

References

- [1] J. C. A. Huang, R. R. Du, C. P. Flynn, *Phys. Rev. Lett.* **66**, 341-344 (1991).
- [2] S. M. Durbin, J. E. Cunningham, C. P. Flynn, *J. Phys. F: Met. Phys.* **12**, L75-L78 (1982).
- [3] Though not strictly a lanthanide, Y is often referred to as a rare earth metal.
- [4] I. Markov, S. Stoyanov, *Contemp. Phys.* **28**, 267-320 (1987).
- [5] E. Bauer, *App. Surf. Sci.* **11/12**, 479-494 (1982).
- [6] E. G. Bauer et al. *J. Mat. Res.* **5**, 852-894 (1990).
- [7] E. Bauer, *Z. Krist.* **110**, 372-395 (1958).
- [8] F. C. Frank, J. H. van der Merwe, *Proc. Roy. Soc. London* **A198**, 205 (1949); F. C. Frank, J. H. van der Merwe, *Proc. Roy. Soc. London* **A198**, 216 (1949); F. C. Frank, J. H. van der Merwe, *Proc. Roy. Soc. London* **A200**, 125 (1950); F. C. Frank, J. H. van der Merwe, *Proc. Roy. Soc. London* **A201**, 261 (1950).
- [9] J. Villain, *J. Phys. I* **1**, 19-42 (1991).
- [10] D.E. Wolf, *Phys. Rev. Lett.* **67**, 1783-1786 (1991).
- [11] M. Volmer, A. Weber, *Z. Phys. Chem.* **119**, 277 (1926).
- [12] I. N. Stranski, L. Krastanow, *Ber. Akademie der Wissenschaften un der Literatur, Mainz. Mathematisch-Naturwissenschaftliche Klasse* **146**, 797 (1939).
- [13] W. K. Burton, N. Cabrera, F. C. Frank, *Proc. Roy. Soc. London* **243**, 299-358 (1950).

- [14] In addition to these basic modes, there are less-common, more complicated modes. A good example is the recent “downward funnelling” model proposed by Evans to explain RHEED intensity oscillations observed for extremely low-temperature growth of metal films on fcc(100) substrates. See, for example, J. W. Evans, D. E. Sanders, P. A. Thiel, A. E. DePristo, *Phys. Rev. B* **41**, 5410-5413 (1990); and J. W. Evans, *Phys. Rev. B* **43**, 3897-3905 (1991).
- [15] A. J. Forty, “Nucleation theory and crystal growth,” in *Surface Science*, (IAEA, Vienna, 1975), vol. 1.
- [16] M. A. Herman, H. Sitter, *Molecular beam epitaxy: fundamentals and current status* (Springer-Verlag, Berlin, 1996).
- [17] R. Du, C. P. Flynn, *J. Phys. C* **2**, 1335 (1990).
- [18] J. E. Ayers, S. K. Ghandhi, L. J. Schowalter, *J. Cryst. Growth* **113**, 430-440 (1991).
- [19] B. Müller, B. Fischer, L. Nedelmann, A. Fricke, K. Kern, *Phys. Rev. Lett.* **76**, 2358-2361 (1996).
- [20] J. W. Matthews, A. E. Blakeslee, *J. Cryst. Growth* **27**, 118 (1974); J. W. Matthews, A. E. Blakeslee, *J. Cryst. Growth* **29**, 273 (1975); J. W. Matthews, A. E. Blakeslee, *J. Cryst. Growth* **32**, 265 (1976).
- [21] K. Nozawa, Y. Horikoshi, *J. J. App. Phys.* **30**, L668-L671 (1991).
- [22] J. S. Whelan, T. George, E. R. Weber, S. Nozaki, A. T. Wu, M. Umeno, *J. App. Phys.* **68**, 5115-5118 (1990).
- [23] M. A. Herman, H. Sitter, *Molecular Beam Epitaxy* (Springer-Verlag, Berlin, 1996).
- [24] E. A. Beam, Y. C. Kao, *J. App. Phys.* **69**, 4253-4262 (1991).
- [25] E. A. Fitzgerald, Y. H. Xie, M. L. Green, D. Brasen, A. R. Kortan, J. Michel, Y. J. Mii, B. E. Weir, *App. Phys. Lett.* **59**, 811-813 (1991).
- [26] S. I. Molina, F. J. Pacheco, D. Araujo, R. Garcia, A. Sacedon, E. Calleja, Z. Yang, P. Kidd, *App. Phys. Lett.* **65**, 2460-2462 (1994).
- [27] J. Tersoff, *App. Phys. Lett.* **62**, 693-695 (1993).
- [28] C. M. Serrano, C. Chang, *App. Phys. Lett.* **39**, 808-809 (1981).

- [29] M. S. Abrahams, C. J. Buiocchi, G. H. Olsen, *J. App. Phys.* **46**, 4259-4270 (1975).
- [30] W. E. Lee, K. P. D. Lagerlof, *J. Elec. Microscopy Tech.* **2**, 247-258 (1985).
- [31] *International Tables for X-ray Crystallography* (Kluwer, Dordrecht, 1992).
- [32] R. R. Du, Ph. D. thesis, University of Illinois at Urbana-Champaign.
- [33] M. Yoshimoto, T. Maeda, T. Ohnishi, H. Koinuma, O. Ishiyama, M. Shinohara, M. Kubo, R. Miura, A. Miyamoto, *App. Phys. Lett.* **67**, 2615-2617 (1995);
- [34] D. W. Susnitzky, C. B. Carter, *J. Am. Ceram. Soc.* **75**, 2463 (1992).
- [35] M. G. Norton, C. B. Carter, *Scanning Microsc.* **6**, 385 (1992).
- [36] M. G. Norton, C. B. Carter, *J. Cryst. Growth* **110**, 641 (1991).
- [37] J. R. Heffelfinger, M. W. Bench, C. B. Carter, *Surf. Sci.* **343**, L1161-L1166 (1995).
- [38] K. Theis-Bröhl, private communication.
- [39] M. Yeadon, M. T. Marshall, F. Hamdani, S. Pekin, H. Morkoc, J. Murray Gibson, *J. App. Phys.* **83**, 2847-2850 (1998).
- [40] P. W. Tasker, in *Structure and Properties of MgO and Al₂O₃ Ceramics*, W. D. Kingery, ed. (American Ceramics Society, Columbus, 1984), p. 176.
- [41] J. Guo, D. E. Ellis, D. J. Lam, *Phys. Rev. B* **45**, 13647-13656 (1992).
- [42] M. L. Kronberg, *Acta Metallurgica* **5**, 507-524 (1957).
- [43] J. C. A. Huang, Ph. D. thesis, University of Illinois at Urbana-Champaign.
- [44] A good measure of the disparity between Nb and Ta, which are otherwise structurally similar, is provided by the anisotropy ratio, defined as $a=c_{44}/(c_{11}-c_{12})$. Values for Ta, Nb, Mo and W are 1.56, 0.51, 0.775, and 1.0, respectively. There is a huge disparity between Ta and Nb, despite their structural similarity. For more information, see J. Hirth, J. Lothe, *Theory of dislocations* (Wiley, New York, 1982).
- [45] S. Durbin, Ph. D. thesis, University of Illinois at Urbana-Champaign.

- [46] G. Gutekunst, J. Mayer, M. Rühle, *Phil. Mag. A* **75**, 1329-1355 (1997); G. Gutekunst, J. Mayer, V. Vitek, M. Rühle, *Phil. Mag. A* **75**, 1357-1382 (1997).
- [47] R. E. Pico, "Titanium sublimation pumping," in *11th Symposium on Fusion Energy Proceedings* (EPRI, Austin, 1985).
- [48] Y. Mei, W. W. Harrison, *Electrochimica Acta B* **46**, 175-182 (1991).
- [49] M. Huth, private communication.
- [50] L. H. Greene, W. L. Feldmann, J. M. Rowell, B. Batlogg, E. M. Gyorgy, W. P. Lowe, D. B. McWhan, *Superlattices Microstruct.* **1**, 407 (1985).
- [51] C. Sürgers, H. v. Loehneysen, *Thin Solid Films* **219**, 69-79 (1992).
- [52] J. Donachie, *Titanium: a technical guide* (ASM, Metals Park, Ohio, 1988).
- [53] See M. Coppel, M. C. Reuter, E. Kaxiras, R. M. Tromp, *Phys. Rev. Lett.* **63**, 632 (1989) for references about surface surfactants.
- [54] An understanding of this growth behavior is made easy by considering the surface atomic potential: along the close-packed direction, there is frequent corrugation of the potential and thus the minima are shallow; normal to the close packed direction, the corrugation is more abrupt and deeper.
- [55] $\text{Ti}_x\text{Zr}_{1-x}$ undergoes a martensitic hcp/bcc phase transition at 882 °C and 863 °C for $X=1$ and $X=0$, respectively; this temperature is reduced to 605 °C for $X=0.5$. See, for example, T. B. Massalski, *Binary alloy phase diagrams* (ASM, Materials Park, Ohio, 1990).
- [56] AFM measurements of ultrasmooth Ti surfaces deposited on C-plane sapphire reveal step heights which are expected if oxidation effects are not deleterious. M. Huth, private communication.
- [57] The XRD measurements were conducted before observing the anisotropic character of the transverse Bragg linewidths. Nevertheless, the observed range of linewidths reported exceeds this anisotropy, except for data in the range near $T = 500^\circ\text{C}$.
- [58] L. Z. Mezey, J. Giber, *J. J. App. Phys.* **21**, 1569-1571 (1982).
- [59] D. S. Gornyi, Al. Tovskiy, *Fiz. Metall. Metalloved* **30**, 85-89 (1970).
- [60] T. B. Massalski, *Binary alloy phase diagrams* (ASM, Materials Park, Ohio, 1990).

- [61] C. P. Flynn, *Point defects and diffusion* (Clarendon, Oxford, 1972).
- [62] U. Leushake, private communication.
- [63] S. Petersen, private communication.
- [64] N. N. Skvortsov, V. A. Skeben, Y. K. Ustinov, S. V. Jalyshko, *Opt. Mekh. Prom.* **2**, 37-39 (1990).
- [65] A. J. Dekker, in *Solid state physics source book*, S. P. Parker, ed. (McGraw-Hill, New York, 1987).
- [66] C. P. Flynn, *J. Phys. F: Met. Phys.* **18**, L195-L200 (1988).
- [67] M. A. Krivoglaz, *Theory of x-ray and thermal-neutron scattering from real crystals* (Dover, New York, 1967).
- [68] P. F. Miceli, C. J. Palmstrom, *Phys. Rev. B* **51**, 5506-5509 (1995).
- [69] G. L. Zhou, Ph.D. thesis, University of Illinois at Urbana-Champaign
- [70] This may explain the long-observed fact that epitaxial bcc(110) crystals on sapphire are always obtained with considerably greater quality than for other orientations.